International Journal of Hydrogen Energy 248 (2026) 155972

Contents lists available at ScienceDirect

International Journal of Hydrogen Energy

journal homepage: www.elsevier.com/locate/he

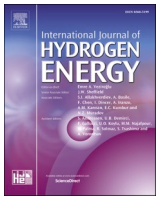

# Aqueous phase reforming of wastewaters from the hydrothermal carbonization of microalgae: tackling the catalyst deactivation challenge via upstream pretreatment

Marina Andriolo, Edoardo Tito, Giuseppe Pipitone *, Raffaele Pirone, Samir Bensaid

*Department of Applied Science and Technology, Politecnico di Torino, Corso Duca degli Abruzzi 24, Turin, 10129, Italy*

ARTICLE INFO

*Keywords:*
Aqueous phase reforming
Biorefinery
Hydrothermal carbonization
Microalgae
Wastewater

ABSTRACT

Aqueous phase reforming (APR) is a promising route to produce hydrogen, but implementation with real feedstocks is limited by rapid deactivation. Here, we report for the first time the APR of wastewater from microalgae hydrothermal carbonization. The effects of carbon concentration and temperature were investigated, with the highest hydrogen productivity obtained at 1.7 $g_C$/L and 270 °C, yielding 13 mmol $H_2/g_C$. Catalyst deactivation was elucidated through an integrated approach: carbon deposition was demonstrated by $N_2$ physisorption analysis and TGA, while inorganic accumulation by XPS and FE-SEM/EDX, pointing to a combined mechanism. Therefore, mitigation strategies were proposed, including thermal pretreatment to avoid solid formation and adsorption of phosphate. Among the options, the latter markedly improved APR up to 30 mmol $H_2/g_C$. Overall, by correlating wastewater characterization with a dual deactivation route, and demonstrating a viable upstream mitigation approach, this study provides a practical basis for improving APR robustness when processing real streams.

## 1. Introduction

Hydrothermal carbonization (HTC) of biomass simulates natural coalification processes to produce a carbon-rich solid product, often named as hydrochar [1]. It occurs at mild temperatures (180-250 °C) and autogenous pressure in a water-rich environment, so that it is particularly convenient when dealing with moisture-rich biomass, such as microalgae [2]. Hydrochar applications range from a solid fuel to soil remediation, for functional materials and as activated carbon [3]. From the pioneering work of Heilmann et al., several research groups investigated mostly the reaction conditions to maximize the hydrochar yield and quality (such as the higher heating value, porosity and functionality) [4–6].

However, hydrochar is not the only obtained product. Depending on the employed operating conditions, up to 20 wt% of the feedstock can end up in the aqueous phase (namely, HTC-AP), which hence needs proper treatment and valorization strategies due to the cost associated with its management [7]. Nguyen et al. recently showed that most of the applications of HTC-AP are in the energy recovery field (e.g., via anaerobic digestion [8,9]), followed by nutrient recovery (e.g., struvite and hydroxyapatite) [10], algae cultivation [7], chemical extraction and carbon source for biological denitrification [11]. One of the complexities associated with its suitable valorization is that deep characterization of the molecules dissolved in the HTC-AP is scarce, to our knowledge [12].

A promising process that has recently attracted attention to valorize the organic carbon content of wastewater streams is aqueous phase reforming (APR) [13]. APR is a catalytic reaction carried out between 220 and 270 °C under pressure to produce hydrogen from biomass-derived compounds dissolved in an aqueous solution [14]. It shows energetic advantage with respect to steam reforming due to the lower operating temperature, the avoidance of water vaporization and the obtainment of pressurized hydrogen. Furthermore, the promotion of water gas shift minimizes the CO content, favoring the use of the gaseous effluent in a proton exchange membrane fuel cell [15].

While most of the literature typically focuses on the optimization of the catalyst formulation starting from simple model compounds [16], there is a growing interest on the direct application of APR to more complex feedstocks. Justicia et al. recently carried out the APR of wastewater from catalytic pyrolysis of woodchips, reporting a production of 23 mmol $H_2/g_{TOC}$ (i.e., molar productivity of $H_2$ expressed per gram of organic carbon present in the fed wastewater) [17]. The authors highlighted the refractory nature of acetic acid in the mixture and the

* Corresponding author.
*E-mail address:* giuseppe.pipitone@polito.it (G. Pipitone).

https://doi.org/10.1016/j.ijhydene.2026.155972
Received 20 February 2026; Received in revised form 17 April 2026; Accepted 7 June 2026
Available online 11 June 2026

moderate decrease in hydrogen production due to gradual adsorption of high molecular weight compounds. However, no insights into inorganic species were provided. Yu et al. explored the use of APR for the treatment of landfill leachate membrane concentrates using Ni-based catalysts, reaching an optimal hydrogen yield equal to ca. 12 mmol $H_2/g_{COD}$ (i.e., molar productivity of $H_2$ per gram of oxygen required to oxidize all carbon in the wastewater) [18]. The authors highlighted that catalyst stability needs further optimization due to pollutant adsorption and carbon deposition. Other works looked, for the sake of example, at pruning waste biomass (max. 17 mmol $H_2/g_{TOC}$) [19], aqueous fractions of pyrolysis bio-oil (max. 40 mmol $H_2/g_{TOC}$) [20], and biogas slurry (max. 3 mmol $H_2/g_{COD}$) [21]. In parallel, system-level studies have emphasized the potential of APR as a valorization route for by-product streams in thermochemical biorefineries, able to improve overall sustainability indicators [22,23].

To the best of our knowledge, microalgae-derived HTC-AP has not yet been investigated as a feedstock for APR. This system introduces the additional complexity associated with N-containing compounds into the APR framework. Moreover, as cited above, the practical deployment of APR with real wastewater remains constrained by catalyst deactivation induced by the feedstock components, which the literature largely attributes to the organic fraction through coke-like formation, underscoring the need for effective pretreatment/operational strategies. By comparison, the contribution of inorganic constituents has received limited attention, even though they may promote poisoning and inorganic fouling.

To address these gaps, in this work we investigated the APR of microalgae-derived HTC-AP, combining an in-depth characterization of the feed with a dedicated assessment of catalyst stability. Based on the results obtained, we proposed and validated an operational strategy aimed at mitigating deactivation and enabling stable catalytic performance.

## 2. Materials and methods

### 2.1. Materials

Glycolic acid and $Ru/Al_2O_3$ were purchased from Sigma Aldrich. $Ru/Al_2O_3$ was selected for its higher activity with respect to a Pt-based catalyst in a preliminary screening (data not shown). The aqueous phase from *Chlorella sorokiniana* HTC (HTC-AP) was kindly provided by CEA, France. Hydrothermal carbonization was performed at 200 °C, with a reaction time of 30 min. The aqueous sample was stored in a refrigerator and filtered with a nylon 0.2 μm filter before use. Unless specified, no further treatments were carried out before testing.

### 2.2. APR tests

The APR catalytic tests have been carried out in a batch reactor (4566 Parr series) equipped with a 4848-model reactor controller (Parr). For each reaction, 75 mL of aqueous phase was prepared and 400 mg of $Ru/Al_2O_3$ was added. The reactor was purged with nitrogen, and the initial pressure was set at 0.3 MPa. The stirring rate was fixed at 400 rpm. The reaction time was set at 1 h, starting once the set-point temperature was reached. The gas phase was collected in a syringe and analyzed by Micro-GC. The liquid phase was recovered from the reactor, filtered by gravity to remove the catalyst, then it was subjected to total organic carbon (TOC), HPLC, gas-chromatography coupled with mass spectroscopy (GC-MS) and ion chromatography (IC) analysis. The solid phase, constituted by the spent catalyst and any insoluble species, was dried overnight in an oven at 105 °C, recovered and weighed. It was hence employed in the reuse tests, without any further treatment after the drying step.

The performance of the APR was estimated using indicators conventionally used in literature. The carbon to gas (CtoG) conversion was defined as the ratio between the moles carbon in the gas product $mol_{fin}C_{gas}$ and the moles of carbon in the feed $mol_{in}C_{feed}$ (Eq. (1)). The hydrogen gas distribution was calculated as the ratio between the moles of hydrogen present in the gas phase as molecular hydrogen ($mol_{fin}\ H_2$) after the reaction and the total moles of hydrogen, including hydrogen contained in alkanes (Eq. (2)); the hydrogen productivity was expressed as the mmoles of hydrogen produced divided by the grams of carbon in the feed (Eq. (3)). This last definition was useful to define a sort of hydrogen yield in the case of complex mixtures with partially unknown compounds, when the definition of a conventional reaction stoichiometry is not applicable. TOC removal was defined as the ratio between the residual and initial TOC in the liquid phase (Eq. (4)). It was reported in addition to CtoG conversion to distinguish the disappearance of dissolved carbon from its recovery as gaseous products and potential solid-phase species formation, defined as carbon to solid conversion (Eq. (5)). The last two indicators were used in the case of glycolic acid reforming: the hydrogen yield, was calculated as the ratio between the moles of produced hydrogen in the gas phase ($mol_{fin}\ H_2$) and the maximum stoichiometric amount that could be produced (Eq. (6)); the conversion of glycolic acid, defined as the ratio between the converted moles of glycolic acid and the moles of feed (Eq. (7)).

$$\text{Carbon to gas conversion } (\%) = 100 \cdot \frac{mol_{fin}C_{gas}}{mol_{in}C_{feed}} \tag{1}$$

$$\text{H}_2\text{ gas distribution } (\%) = 100 \cdot \frac{mol_{fin}H_2}{mol_{fin}(H_2 + 2{\cdot}CH_4 + 3{\cdot}C_2H_6 + 4{\cdot}C_3H_8)} \tag{2}$$

$$\text{H}_2\text{ productivity} = \frac{mmol_{fin}H_2}{g_{in}C_{feed}} \tag{3}$$

$$\text{TOC removal } (\%) = 100 \cdot \frac{TOC_{in} - TOC_{fin}}{TOC_{in}} \tag{4}$$

$$\text{Carbon to solid conversion } (\%) = 100 \cdot \frac{g_{in}C_{feed} - g_{fin}C_{gas} - g_{fin}C_{liq}}{g_{in}C_{feed}} \tag{5}$$

$$\text{H}_2\text{ yield } (\%) = 100 \cdot \frac{mol_{fin}H_2}{3{\cdot}mol_{in}glycolic} \tag{6}$$

$$\text{Conversion}_{\text{glycolic}} (\%) = 100 \cdot \frac{mol_{in}glycolic - mol_{fin}glycolic}{mol_{in}glycolic} \tag{7}$$

### 2.3. Adsorption pretreatment

A selective adsorption via ion-exchange was carried out on the wastewater to investigate the influence of inorganic species (namely sulfate and phosphate). Amberlite IRA-67, a commercial weak base anion exchange resin with a gel-type acrylic matrix, was employed. This choice was specifically motivated by the nature of the resin, since, unlike those used in another study [24], it was employed in its free-base form [25], allowing ion exchange to occur between inorganic ions and hydroxide ions ($OH^-$). The aqueous phase volume was 100 mL, and the amount of Amberlite IRA-67 varied to reach the desired adsorption efficiency for specific components. The solution was stirred using a mechanical agitator equipped with a magnetic stir bar. Samples were periodically collected and analyzed by ion chromatography to measure the inorganics concentration.

### 2.4. Analytical methods

#### 2.4.1. Product analysis

The gas phase was analyzed by an SRA Micro-GC, equipped with Molsieve 5A and PoraPLOT U Columns, with a TCD detector.

HPLC analysis (Shimadzu) was performed with a Rezex ROA-Organic acid $H^+$ (8%) column (300 mm × 7.8 mm). The mobile phase was a

5 mM $H_2SO_4$ aqueous solution. The flow rate was fixed at 0.7 mL/min and the temperature of the column at 50 °C. The products were determined by means of a refractive index detector (RID).

Total carbon (TC) and total organic carbon (TOC) analysis were performed using a Shimadzu TOC-$V_{CSH}$ analyzer equipped with a nondispersive infrared detector.

GC-MS (Agilent 7890A GC–5975C MS) analysis was conducted to refine the identification of the molecules dissolved in the aqueous solutions. Without any prior derivatization and dilution, 1 μL of syringe-filtered sample was injected into a DB-WAX Ultra Inert column (30 m × 0.25 mm × 0.25 μm) in splitless mode with an injection temperature of 240 °C. The helium flow was set at 1 mL/min, using the following temperature program: 80 °C (0 min hold) followed by a heating ramp of 5 °C/min up to 250 °C (0 min hold). Compounds were identified using Agilent MassHunter Unknown Analysis software with the NIST 17 library and only compounds with a match factor greater than 70 were considered.

A Thermo Scientific Inuvion system equipped with an IonPac AS11-HC-4 column, KOH eluent generation and suppressed conductivity detector was employed to determine the anions present in the aqueous phase. The eluent flow was set at 1.5 mL/min and the temperature at 30 °C.

Inductively coupled plasma-mass spectrometry (ICP-MS) was employed for the identification and quantification of additional elements. A Thermo Scientific iCAP RQ-MS was used to conduct the analysis.

#### 2.4.2. Catalyst characterization

A Micromeritics Tristar 3020 instrument was used to measure the $N_2$ adsorption/desorption isotherms of the fresh and spent catalysts at 77 K. The samples were pretreated at 200 °C under nitrogen flow for 2 h through a Micromeritics Flow Prep 060 degassing system. The specific surface area was calculated according to the Brunauer-Emmet-Teller (BET) equation. Thermogravimetric analysis (TGA, Mettler Toledo SDTA851) was performed to evaluate possible carbon deposition phenomena on the spent catalysts. Approximately 20 mg of sample was heated from 25 °C to 900 °C at 10 °C/min under an argon flow of 50 mL/min. Once the final temperature was reached, the carrier gas was switched to air (50 mL/min) and the temperature was maintained at 900 °C for 5 min. Field-emission scanning electron microscopy (FE-SEM) analyses were carried out using a Zeiss Merlin microscope (imaging mode, 3 kV), equipped with a Gemini II column; elemental composition was determined by EDX with an Oxford detector at an accelerating voltage of 15 kV. The structural features of the catalysts were examined by X-ray diffraction (XRD) using a PANalytical X'Pert diffractometer with Cu Kα radiation. Diffraction patterns were recorded over $20° \leq 2\theta \leq 80°$ at a scanning rate of 2.0°/min. X-ray photoelectron spectroscopy (XPS) measurements were carried out using an Omicron Argus spectrometer equipped with a monochromated Al Kα X-ray source ($h\nu = 1486.6$ eV). Binding energy calibration was performed by setting the Al 2p component at 74.6 eV. Attenuated total reflectance Fourier-transformed infrared spectroscopy (ATR-FTIR) was performed using a Bruker Tensor 27 spectrometer. Spectra were collected in the range of 4000–400 $cm^{-1}$ at a resolution of 2 $cm^{-1}$, and were subsequently postprocessed using the baseline correction tool in OPUS software. An elemental analyzer (Elementar Vario Macro Cube) was used to determine the elemental composition (CHNS) of spent catalysts.

## 3. Results and discussion

For clarity, the section is organized into four main parts. Section 3.1 presents the characterization of the HTC-AP, providing the basis for the subsequent catalytic investigation. Section 3.2 focuses on the APR performance, starting from the analysis of operating conditions (initial carbon concentration and reaction temperature), followed by the assessment of catalyst deactivation. Section 3.3 investigates the influence of different pretreatment strategies aimed at mitigating deactivation, together with their impact on catalyst stability. Finally, Section 3.4 reports the characterization of fresh and spent catalysts, in order to correlate catalytic performance with structural and surface properties.

### 3.1. Characterization of the hydrothermal carbonization aqueous phase

The TOC content was determined to be 30.8 ± 0.5 g/L, a value consistent with those reported in the literature [26,27]. As cited in the introduction, the characterization is complex, and different techniques should be used to derive proper information. HPLC analysis allowed to quantify the main organic components, including glycerol (6800 $ppm_w$), acetic acid (4700 $ppm_w$), propionic acid (2300 $ppm_w$), and 5-hydroxymethylfurfural (5-HMF) (2200 $ppm_w$), as shown in Fig. 1-A. Additional peaks were observed in the early-eluting region (retention time 6–11 min) and were mainly assigned to sugar-like compounds. This attribution is supported by the retention times of sugars external standards analyzed under identical conditions (Fig. S1–A) and it is consistent with the chromatographic behavior of the employed method, for which highly polar carbohydrates elute at low retention times [28–30]. Furthermore, it is supported by their marked conversion in non-catalytic tests (as will be reported in Section 3.3.1), in agreement with the well-known hydrothermal instability of carbohydrates under the applied conditions. Notably, one peak, with a retention time at about 7.5 min, was labelled as "unknown" and not grouped with the sugar-like signals. Unlike the other early-eluting peaks, it remained essentially unchanged in the non-catalytic test, indicating higher thermal stability than a sugar compound. Moreover, its PDA spectrum was more consistent with that of a carboxylic acid rather than a carbohydrate-like species, showing an adsorption peak at approximately 195 nm. To support this assignment, several common short-chain carboxylic acids were analyzed as external standards, but no match was identified (Fig. S1–B). Although glucuronic and maleic acids exhibited retention times close to that of the unknown peak, they were excluded based on the different PDA spectral fingerprints. The use of additional techniques, such as HPLC-MS, is planned to allow for its identification.

The aqueous sample was further analyzed by GC-MS (chromatogram in Fig. S2) to expand the compositional analysis beyond the subset of compounds confidently identified and quantified by HPLC (i.e., those covered by the available external calibration standards). The identified components were categorized into groups according to their functional characteristics. It should be noted that compounds containing more than one functional group were classified into a single category. In particular, the following classes were identified: pyrroles, pyridines, pyrazines, 5-HMF, other aromatics, lactams, amides, other N, lactones, acids, cyclic ketones, ketones, oxygenated compounds (including ethers, esters, alcohols, and aldehydes). In cases where multiple functional groups were present, the above order of priority was used to assign each compound to its corresponding family. The relative proportions of these classes and the complete list of the compounds are shown in Fig. 1-B, Table S1 and Table S2. It is important to note that the most abundant class of compounds identified was related to carboxylic acids, with acetic and propionic acid being the most prevalent ones. Similarly, HTC-AP of the microalga *N. Oculata*, was dominated by acetic acid, followed by lactic acid, citric acid and glycerol, based on HPLC and GC-MS analyses [31]. Unlike the observation of Broch et al. [11] 5-HMF was particularly notable among the detected compounds, and it is a known product of the hydrothermal carbonization of cellulose and hemicellulose, as its precursors are six-carbon sugars [32,33]. Moreover, based on normalized GC-MS peak areas, approximately 20% of the compounds identified by GC-MS were characterized by the presence of a nitrogen-containing functional group and the most abundant included 3-pyridinol, 6-methyl-3-pyridinol, pyrazine, acetamide and 2-pyrrolidinone. These results are consistent with the studies of Maddi et al. [34] and Gai et al. [35], who suggested that such compounds result from the degradation of

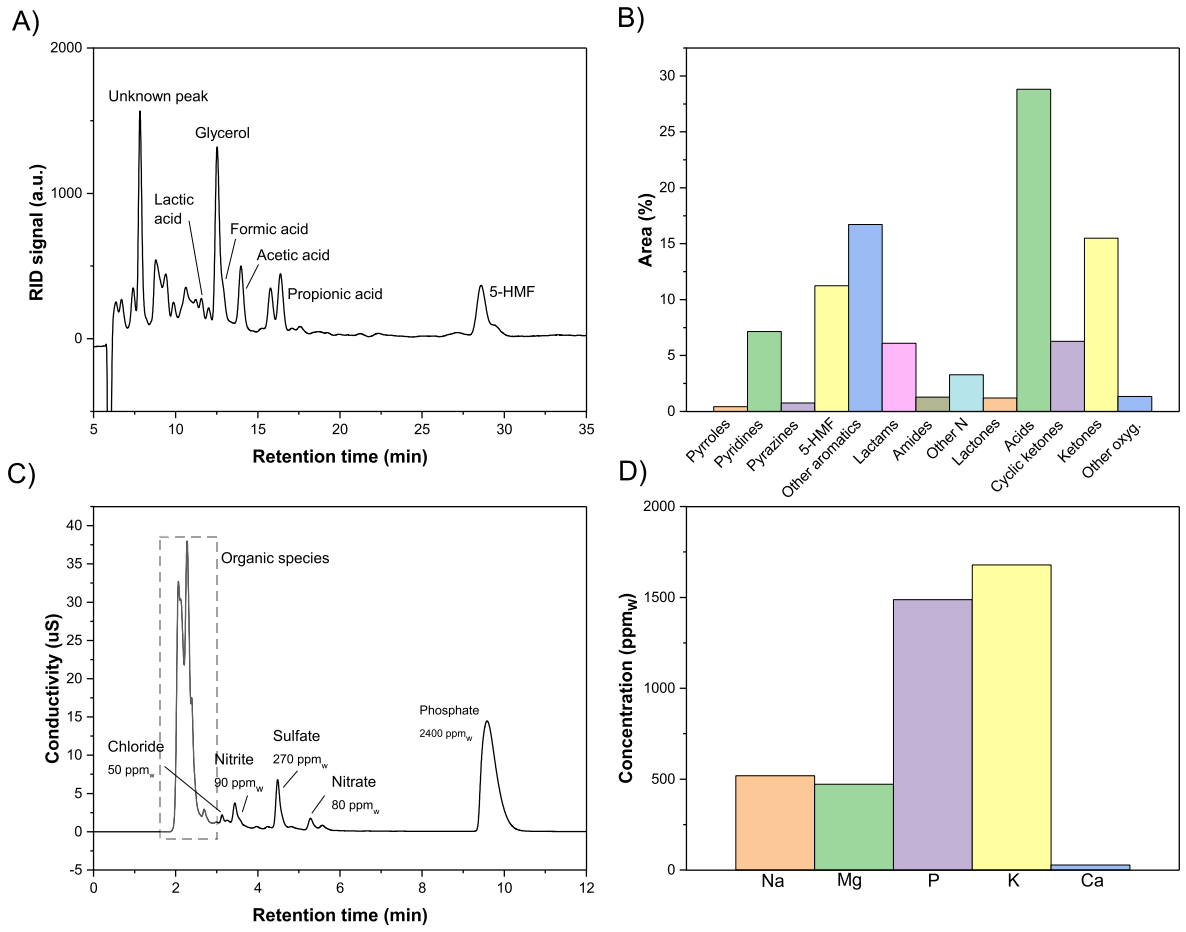


**Fig. 1.** HPLC chromatogram of the HTC-AP and concentration of the main identified compounds (A); Families of compounds identified after GC–MS (B); IC chromatogram and concentration of the main identified anions (C); Ion concentrations identified by ICP analysis (D).

proteins and their amino acids during hydrothermal treatment.

An additional analysis was conducted to assess the presence of inorganic species in the aqueous phase, using ion chromatography (IC). This is particularly relevant for APR, as inorganic species may interact with the catalyst and contribute to its deactivation [36]. Notable concentrations of sulfate and phosphate ions were detected, corresponding to 265 and 2380 mg/L, respectively (Fig. 1-C). Tsarpali et al. reported a phosphate concentration of 1750 mg/L subsequent to HTC of *P. Oculatum* after lipid extraction [26]. Barreiro et al. evaluated the concentration of ions in the aqueous phase obtained from the HTC of *Nannochloris gaditana* and *Scenedesmus almeriensis*, finding sulfate concentrations of approximately 400 mg/L in both cases, and a higher phosphate amount of 4500 mg/L in the sample deriving from marine microalga [37].

Finally, ICP analysis enabled the identification of the major cations present in the aqueous phase: potassium (1679 $ppm_w$), phosphorus (1488 $ppm_w$), sodium (518 $ppm_w$), and magnesium (472 $ppm_w$) (Fig. 1-D).

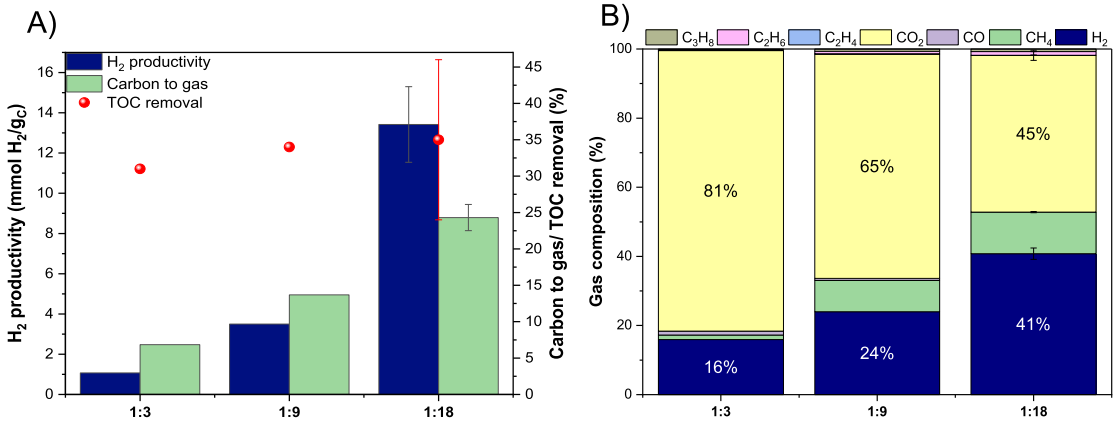


**Fig. 2.** $H_2$ productivity, carbon to gas conversion, TOC removal (A) and gas composition (B), obtained from the APR of HTC-AP at different dilution ratio. Reaction conditions: 400 mg $Ru/Al_2O_3$, 270 °C, 1 h.

### 3.2. Aqueous phase reforming tests

#### 3.2.1. Influence of initial carbon concentration

In this section, the influence of initial TOC (10, 3.4, 1.7 g/L) was studied, maintaining a reaction temperature of 270 °C. These concentrations corresponded to different dilution ratios, specifically 1:3, 1:9 and 1:18. The values of $H_2$ productivity and carbon to gas conversion are reported in Fig. 2-A. At a dilution ratio of 1:3, the $H_2$ productivity was equal to 1 mmol $H_2/g_C$; in contrast, at a dilution ratio of 1:18, the reaction resulted in a hydrogen productivity of 13 mmol $H_2/g_C$ and a CtoG of 24%. These quantitative results are consistent with those reported by Oliveira et al. [38], one of the few studies addressing the coupling of HTC and APR. In their work, APR was performed on the HTC-AP using different catalysts. Under optimal HTC conditions and with a Pt/C catalyst, hydrogen productivity of approximately 9 mmol $H_2/g_C$ was achieved, with an initial TOC of 0.5 g/L. The influence of the initial carbon content was also examined by Torres et al. [19], who observed that lower initial TOC led to improved hydrogen production performance. This trend may be attributed to the promotion of condensation and other side reactions when the organic concentration is increased [19,39] and, as discussed later, to a more pronounced catalyst deactivation occurring at increased TOC levels. Fig. 2-B shows the composition of the gas phase obtained from the APR reaction as a function of the dilution ratio. An increase in dilution led to higher percentages of hydrogen and methane produced, reaching 41% and 12%, respectively, at a dilution ratio of 1:18. In the gas phase obtained from the two most concentrated feeds, CO was detected at 1% (1:3) and 0.6% (1:9), indicating a slightly lower catalytic activity toward the water gas shift reaction.

TOC removal was not significantly affected by changes in the dilution ratio, maintaining a value above 30% (Fig. 2-A). The TOC removal from the aqueous phase is not coherent with the CtoG shown above, indicating that a fraction of the carbon was deposited as a solid phase. This discrepancy also provides insight into the conversion pathways of sugars and aldehydes present in the feed. While these species may in principle undergo conversion to gaseous or soluble products during APR, the limited CtoG (approximately 7% under the most concentrated condition) and the absence of significant new compounds detected by HPLC and GC-MS indicate that these pathways are not dominant. Instead, the missing carbon is primarily accounted for by the formation of insoluble solid products. In our case, both the liquid phase and spent catalyst analysis were essential to better understand the performance trends of the reaction. HPLC analysis revealed that the composition of the liquid phase varied according to the initial dilution ratio. In all tests, 5-HMF was completely converted. This compound, generated during HTC from cellulose and hemicellulose, is among the species implicated in solid residue formation under hydrothermal conditions; importantly, it was completely consumed even under non-catalyzed conditions, indicating that its conversion can proceed via purely thermal pathways (see Section 3.3.1), supporting the hypothesis that sugar-derived compounds are preferentially converted into soluble solids rather than gaseous or soluble products. On the other hand, acetic and propionic acid showed no detectable conversion, consistently with previous studies. This behavior was attributed to kinetically unfavorable reforming pathways [40], together with competitive adsorption phenomena which may arise under aqueous conditions, where carboxylate species showed limited adsorption on metal sites in the presence of more reactive oxygenates [41]. The effect of dilution was particularly evident in the conversion of glycerol, which reached the highest value (68%) for the feed with the highest dilution ratio, in contrast with the negligible conversion obtained in the test with a 1:3 dilution ratio. Regarding N-containing compounds, pyridinols (6-methyl-3-pyridinol and 3-pyridinol) showed partial conversion, which increased with the dilution ratio and reached 50%. In contrast, 2-pyrrolidinone was completely converted under all investigated conditions, whereas acetamide showed no detectable reactivity. In addition, the conversion of 3-methyl-1, 2-cyclopentanedione also increased with dilution ratio, reaching a maximum value of 73%. An ion chromatography analysis was carried out to assess how the concentrations of anions in solution varied following the APR reaction. Nitrate and phosphate ions were completely removed, showing no detectable concentrations in the aqueous phase after the reaction, while sulfates remained unchanged. Their effect will be extensively discussed in Section 3.3.2.

The main hypothesis regarding the improved performance under more diluted conditions is related to the reduced formation of solid deposits during the reaction, which led to a lowered deactivation of the active sites [39,42–45]. Clear evidence of this effect was provided by the state of the impeller and the post reaction solid morphology following APR (see Fig. S3). This phenomenon was more evident under reaction conditions with higher feed concentrations. For this experiment, a carbon to solid conversion of 24% was obtained, corresponding to a theoretical production of 188 mg of carbonaceous solid. A total solid mass of 571 mg was collected at the end of the reaction, but this value includes the amount of catalyst used during the reaction. Considering a catalyst recovery efficiency of ca. 90%, as determined from blank reference tests, the amount of solid obtained at the end of the test confirmed the theoretical estimate derived from the solid to carbon conversion. CHNS analysis of the spent catalyst revealed a carbon content of 17 wt%, corresponding to approximately 94 mg of carbon retained on the catalyst surface, and leading to an overall carbon balance closure of 88%. For the experiments conducted with more diluted aqueous phases (1:9 and 1:18), the carbon to solid conversions were 20% and 11%, corresponding to theoretical productions of 42 mg and 14 mg of solid carbon, respectively. In these cases, the experimental solid recovery remained similar, with total masses of 383 mg and 368 mg, including the catalyst. Given the relatively small contribution of solid carbon compared to the catalyst, its effect on the total recovered mass was not easily distinguishable. Consequently, the influence of dilution on solid carbon formation was less evident in terms of the experimentally recovered solid. These data clearly indicate that solid formation under more concentrated conditions was significantly higher, leading to catalyst deactivation. The subsequent activity of the spent catalysts was investigated in Section 3.2.3.

#### 3.2.2. Influence of temperature

In this section, the influence of the reaction temperature in the range 230-270 °C is discussed, maintaining a feed dilution ratio of 1:18. Fig. 3-A shows the trend of $H_2$ productivity and carbon conversion to gas. As the temperature was raised, the amount of hydrogen produced at 270 °C increased, reaching a value four times higher than the one obtained at 230 °C. The CtoG also increased with temperature, reaching 25% at 270 °C, due to the promoted breaking of C–C bonds, which led to the formation of gaseous products. The gas phase obtained, whose composition is depicted in Fig. 3-B, was mainly constituted of $CO_2$. However, its percentage decreased as the temperature increased, indicating that temperature promoted both a higher conversion and a higher selectivity to hydrogen. This trend was reflected in the behavior of the $H_2/CO_2$ ratio, being 0.41 at 230 °C, 0.60 at 250 °C, and 0.95 at 270 °C. Methane, unlike ethane, ethylene, and propane, showed a slight increase in the gas phase with increasing temperature, from 11% to 14%. This trend was also observed in the lower heating value (LHV) of the gas. With increasing reaction temperature, the LHV rose from 6.32 MJ/$Nm^3$ at 230 °C to 7.55 MJ/$Nm^3$ at 250 °C, reaching 8.71 MJ/$Nm^3$ at 270 °C. These results further confirmed the positive effect of temperature on the energetic quality of the gas phase produced by APR.

Looking at the liquid phase, higher TOC removal was achieved at higher temperatures (17% at 230 °C, 27% at 250 °C, and 43% at 270 °C). 5-HMF was completely converted, unlike acetic acid and propionic acid, which showed a slight increase following the APR reaction. We speculate that the conversion of larger oxygenated compounds can lead to the formation of smaller and more stable carboxylic acids, resulting in higher concentrations of these compounds in the liquid product than in

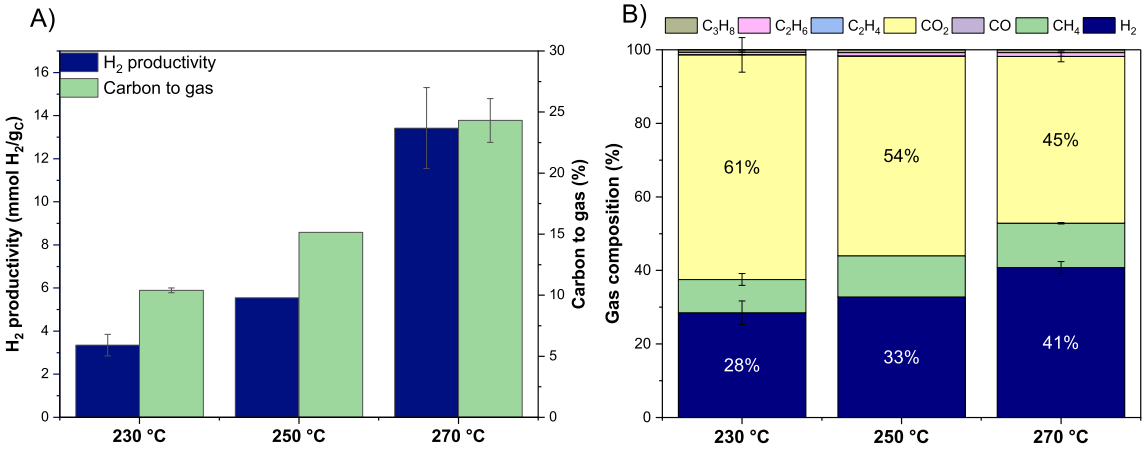


**Fig. 3.** $H_2$ productivity, carbon to gas conversion (A) and gas composition (B), obtained from the APR of HTC-AP at different reaction temperatures. Reaction conditions: 400 mg $Ru/Al_2O_3$, 1 h, 1:18 dilution ratio.

the feed [38]. With increasing temperature, glycerol conversion also increased, from a minimum of 18% at 230 °C, to 25% at 250 °C, and finally to 68% at 270 °C. Being glycerol the most abundant component identified and substantially converted, we assessed whether $H_2$ production could be predominantly attributed to glycerol APR. To this end, the theoretical $H_2$ yield was estimated from the converted glycerol using the stoichiometric APR equation (Eq. (8)).

$$Glycerol + 3\,H_2O \rightarrow 3\,CO_2 + 7\,H_2 \quad (8)$$

As reported in Table S3, at 230 °C, approximately 75% of the measured hydrogen could be accounted for by glycerol APR. Under the other conditions investigated, this ratio decreased to 50-70%. Notably, the 1:3 test showed negligible glycerol conversion yet still produced measurable $H_2$, indicating that additional reaction pathways contributed to gas formation. Overall, these findings demonstrate that glycerol is a major, but not exclusive, source of hydrogen, and that other constituents of the HTC-AP can contribute depending on specific reaction conditions (see Table S2 and Fig. S4).

GC-MS analysis enabled a comparison between the classes of compounds present in the feed and those in the liquid products obtained after the APR reaction. A reduction in oxygenated compounds (ethers, esters, alcohols, and aldehydes) was observed, which became more pronounced with increasing temperature, in agreement with HPLC outcomes. N-containing compounds exhibited partial conversion, increasing with temperature, while acetamide remained unreacted. Ion chromatography analysis did not reveal significant differences across the reaction temperatures. Moreover, no appreciable variations were observed in solid carbon formation, since the amount of solid phase collected after the reaction was comparable across the three experiments (approximately 380 mg). This outcome seemed not consistent with the findings of a previous study [39], where a reduction in solid formation was experimentally observed with increasing reaction temperature, attributed to sugar decomposition. This result could be attributed to the lower carbon concentration employed herein. Therefore, the reaction conditions that led to the best APR performance were a more diluted feed and a temperature of 270 °C.

### 3.2.3. *Assessment of catalyst deactivation: glycolic acid APR tests*

All spent catalysts were tested in a subsequent APR run using glycolic acid as a reference compound to probe the deactivation mechanism. The choice of using a probe molecule, rather than preparing a fresh HTC-AP solution, was motivated by the need for a more sensitive assessment of deactivation, achieved by tracking changes in $H_2$ production under inherently high-performance conditions. Glycolic acid was selected as a reference compound due to its well-documented reactivity in APR and its ability to provide reproducible hydrogen yield without introducing significant additional deactivation pathways [40,46], thus enabling a reliable comparison between fresh and spent catalysts. Fig. 4 reports the results for the spent catalysts derived from the tests described above and compares their behavior with the one obtained with fresh $Ru/Al_2O_3$.

The data clearly show that exposure to HTC-AP during APR induced a significant decline in $Ru/Al_2O_3$ activity. The behavior observed with glycolic acid was fully consistent with the trends identified in the APR of HTC-AP: the lowest hydrogen productivity, carbon to gas and glycolic acid conversions were associated with catalysts that had been used in reactions with more concentrated feeds. Specifically, with the 1:3 dilution, the hydrogen productivity reached only 3 mmol $H_2/g_C$, with a glycolic acid conversion of 3%, in comparison with about 47 mmol $H_2/g_C$ and 90% conversion obtained with the fresh one. These results suggest that the solid formed during the APR of HTC-AP largely deactivated the catalyst.

Increasing the dilution ratio progressively improved the reaction performance, with the spent catalyst recovered from the 1:18 test reaching a hydrogen productivity corresponding to half of that achieved with the fresh catalyst. On the other hand, the different APR temperatures did not seem to influence the extent of catalyst deactivation, being the indicators comparable across the tested conditions. These

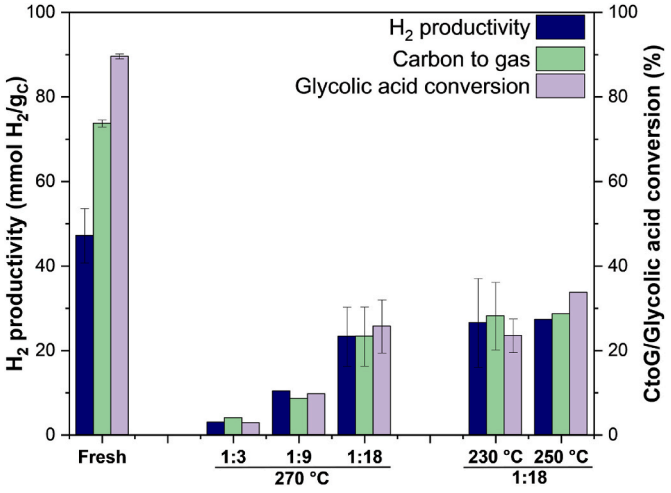


**Fig. 4.** $H_2$ productivity, carbon to gas and glycolic acid conversion obtained from APR reactions of glycolic acid performed with fresh and different spent catalysts. Reaction conditions: 100 mg $Ru/Al_2O_3$, 270 °C, 1 h, 1 wt% glycolic acid.

observations suggest that deactivation is not primarily driven by thermal severity under the applied conditions, but rather by feedstock-derived effects, as will be deepened later.

It is worth noting that a deviation was present between the glycolic acid conversion and the corresponding hydrogen productivity compared with the values obtained with the fresh catalyst. Specifically, while the hydrogen productivity decreased by 50% (comparing the fresh and 1:18 tests), the conversion was substantially more inhibited, with a 71% drop. This finding implies that the hydrogen generated during the reuse tests did not originate solely from the APR of glycolic acid. Rather, it was likely that during the interaction between the catalyst and the HTC-AP, some compounds deposited on the catalyst surface reacted in the presence of glycolic acid, ultimately contributing to the additional hydrogen production. Considering the conversion value, 58 mmol $H_2$ were produced per gram of converted carbon using fresh catalyst, with respect to the 45 mmol $H_2$ produced per gram of initial carbon. This parameter remained the same in the case of the spent catalysts, suggesting that, for all reactions performed, only a fraction of the hydrogen produced, ranging from a minimum 50% to a maximum of 70%, can be attributed to the APR of glycolic acid.

Based on the observed results, two mitigation strategies were investigated. First, being observed fouling phenomena, a thermal pretreatment step was introduced to shift solid formation upstream of the catalytic step, thereby limiting in situ generation that may contribute to deactivation. However, since catalyst deactivation was still observed even under more diluted conditions, where solid formation was comparatively limited, we also examined an alternative and potentially concurrent deactivation route. As will be discussed in Section 3.4, spent-catalyst characterization revealed the accumulation of inorganic species on the catalyst surface. Accordingly, a second pretreatment strategy was investigated, consisting of upstream adsorption to selectively remove inorganic components from the aqueous phase prior to APR.

### 3.3. Influence of pretreatment

#### 3.3.1. Preheating

The performance trends discussed above indicate that higher TOC promoted the formation of insoluble solids during APR, and that these solids were associated with severe catalyst deactivation. This observation suggests that a substantial fraction of solid formation may originate from homogeneous hydrothermal reactions in the liquid phase rather than from strictly catalytic pathways. On this basis, we evaluated a thermal pretreatment, namely preheating, with the purpose of shifting solid formation upstream of the catalyst and thereby mitigate in situ deposition and deactivation. The pretreatment was carried out by heating the aqueous feed with dilution ratios of 1:3 and 1:18 to the target reaction temperature (270 °C) for 1 h, without addiction of any catalyst. Under these conditions, the preheating step can be regarded as an additional hydrothermal treatment of the aqueous phase, analogous to an HTC process. The gas produced during preheating at both dilution ratios consisted mainly of $CO_2$, 95% and 85% respectively, and $H_2$, leading to $H_2/CO_2$ ratios of 0.02 and 0.12 (data not shown). CO was also detected, a result that can be attributed to the occurrence of the hydrothermal carbonization process under these conditions, and the lack of efficient water gas shift [41].

Table 1 shows that TOC removal was higher for the more concentrated feed in the preheating step, reaching approximately 31%, with a carbon to gas conversion of about 7%. On the other hand, the 1:18 test reported similar CtoG, but threefold lower TOC removal. The discrepancy can be explained looking at the amount of solid recovered, which was 104 mg for the 1:3 test, and negligible for the 1:18. CHNS analysis of this solid fraction indicated a carbon content of 60 wt%, corresponding to approximately 63 mg of carbon and resulting in an overall carbon balance closure of 84%. These results confirm the hypothesis that solid formation was governed by carbon loading. FTIR spectra of the obtained solid (Fig. S5–C) presented peculiar bands associated with O–H bonds of carboxylic and hydroxyl groups at about 3400 $cm^{-1}$, C–O–C stretching band associated with carbohydrate-derived origin at about 100 $cm^{-1}$, and C═C, C═O and N–H functional groups of aromatic and amide at approximately 1400-1700 $cm^{-1}$ [47]. Moreover, peaks in the 700-800 $cm^{-1}$ region may be associated with phenolic or furanic structure [48]. While it is difficult deriving a formation mechanism, the presence of such groups indicates the strong role played by aldol condensation and Maillard reaction [49]. HPLC analyses performed on samples collected during the preheating step indicated the disappearance of peaks associated with sugar compounds, as well as the peak corresponding to 5-HMF (see Fig. S5). These observations were further supported by GC-MS analysis, which confirmed the depletion of key furanic intermediates, including 5-HMF and 2,5-dimethylfuran-3,4(2H, 5H)-dione. These compounds are well-known products of sugar degradation and are prone to condensation and polymerization reactions leading to the formation of solid carbonaceous materials [50,51]. Their consumption during preheating supported the hypothesis that sugar species may have contributed to solid carbon formation under the investigated conditions [39,52]. In contrast, IC analysis did not reveal significant changes in the concentration of inorganic species in the liquid phase after thermal pretreatment, indicating that this step did not effectively remove potential inorganic foulants.

**Table 1**
TOC removal, CtoG, theoretical solid carbon and experimental solid phase from APR reactions of HTC-AP at different dilution ratio. Preheating conditions: 270 °C, 1 h; Reaction conditions: 400 mg $Ru/Al_2O_3$, 270 °C, 1 h.

| Test (Dilution ratio) | | TOC removal (%) | Carbon to gas (%) | Theoretical solid carbon[a] (mg) | Experimental solid phase[b] (mg) |
|---|---|---|---|---|---|
| 1:3 | Preheating | 30.9 | 6.8 | 181.0 | 104.0 |
| 1:18 | Preheating | 8.9 | 7.6 | 3.8 | 4.3 |
| 1:3 | Reaction | 15.4 | 4.5 | 45.8 | 435.0 |
| 1:18 | Reaction | 39.0 | 30.7 | 7.2 | 381.0 |

[a] Theoretical solid carbon assuming a complete carbon balance.
[b] Solid actually recovered after APR reaction.

Following the preheating step, the APR reactions were carried out using 400 mg of $Ru/Al_2O_3$ catalyst, and the obtained results are presented in Fig. 5. Please note that, in these experiments, the reported values were calculated based on the actual TOC present before the reaction step. With regards to the 1:3 dilution ratio, the hydrogen productivity doubled, while the carbon to gas conversion decreased to 4.5% (Fig. 5-A). In terms of gas phase composition (Fig. 5-B), the preheating step led to a gas richer in hydrogen and methane compared to the untreated case, achieving an $H_2/CO_2$ ratio of 1.02 and no detectable CO. These findings suggest that the thermal treatment effectively promoted APR reaction and reduced catalyst deactivation. In order to exclude a pure dilution effect, an additional APR experiment without pretreatment was carried out using the untreated feed at a dilution ratio of 1:4.3, with a carbon content equal to 6 g/L, approximately corresponding to the TOC of the preheated solution originally diluted at 1:3. Under these conditions, comparable hydrogen productivity was obtained (2.2 mmol $H_2/g_C$), while the gas-phase composition showed significant differences (70% $CO_2$, 26% $H_2$, 4% $CH_4$). This indicates that hydrogen productivity alone provides a limited representation of the effect of thermal pretreatment, given the low absolute value; whereas, the gas-phase composition more directly reflects changes in the reaction network, highlighting a more pronounced effect of thermal pretreatment on product distribution and suggesting that preheating affected the reaction pathways through modifications in the liquid-phase composition rather than through a simple dilution effect. For the more diluted HTC-AP, hydrogen productivity reached 22 mmol $H_2/g_C$, almost doubling the value obtained in the absence of pretreatment. Similarly, the carbon conversion to gas increased, reaching 31%. The gas composition showed slightly higher hydrogen and methane contents at the expense of carbon

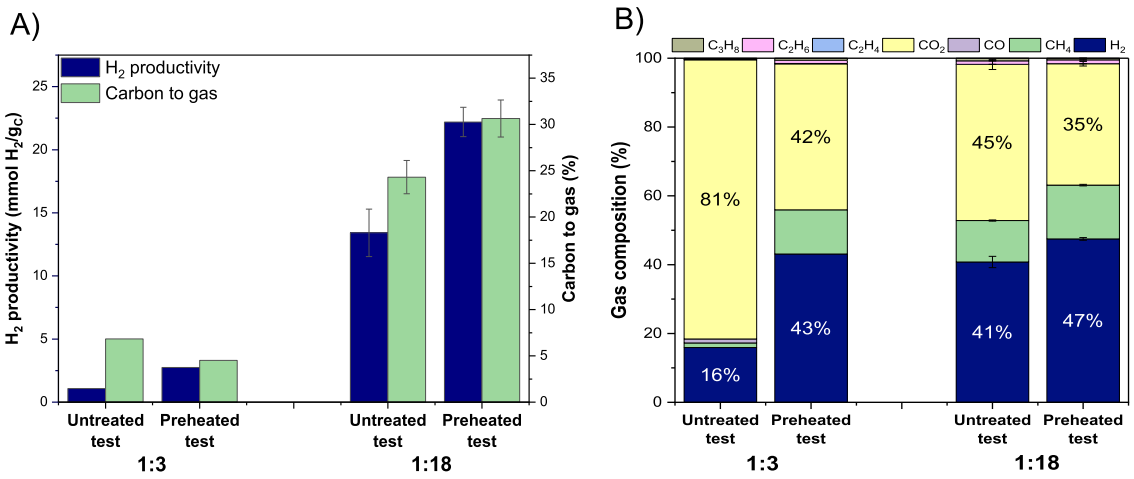


**Fig. 5.** $H_2$ productivity, carbon to gas (A) and gas composition (B) obtained from the APR of HTC-AP. Reaction conditions: 400 mg $Ru/Al_2O_3$, 270 °C, 1 h, 1:3 and 1:18 dilution ratio, without and with preheating.

dioxide. In addition to looking at these two steps (preheating and reaction) in an independent way, it may be valuable elaborating on global indicators, which take into account the hydrogen productivity and carbon to gas with respect to the initial carbon loading (and not only to the carbon fed at each stage). Fig. S6 shows that this two-stage approach increased both hydrogen productivity and CtoG with respect to the one-pot reaction across all dilution ratio investigated. Notably, at the highest concentration, the CtoG in the preheating stage was similar to that of the one-pot reaction, suggesting the minimal role of the catalyst in this operating condition. Furthermore, focusing on the reaction stage of both tests, the presence of the preheating step enhanced hydrogen production, despite a lower overall CtoG resulting from the substantial fraction of carbon already removed during pretreatment.

For the reaction carried out at a 1:3 dilution ratio, a TOC removal of 15% was achieved. Notably, the effect of thermal treatment can be clearly seen in glycerol conversion, which reached 33%, while it did not show detectable conversion without pretreatment. Ion chromatography revealed that, consistent with previous experiments, sulfate remained unchanged, whereas nitrates were completely absent and phosphates were detected at 5 ppm (96% reduction). Based on this result, and as further elaborated below, the role of phosphate concentration in deactivation could not be excluded. Despite thermal treatment, solid formation still occurred during the reaction carried out at 1:3 dilution ratio. This was evidenced by the mass of recovered solids, exceeding 400 mg. CHNS analysis of the spent catalyst showed a carbon content of 4 wt%, reflecting a reduced carbon accumulation on the catalyst surface and leading to an overall carbon balance closure of 93%.

At 1:18 dilution ratio, APR resulted in a 39% removal of TOC. Under these conditions, glycerol was fully converted from the aqueous phase (vs 68% in the untreated feed), while acetic and propionic acids again showed no detectable conversion. No significant differences were observed in the GC-MS and IC analysis with respect to the tests conducted without pretreatment. Finally, it is worthy noting that the improved APR performance observed after pretreatment cannot be ascribed merely to a longer overall processing time, since only a fraction of the original catalyst activity could be maintained after the first hour, as derived from Fig. 4.

### 3.3.2. *Sulfate and phosphate adsorption*

Sulfur is one of the main causes of poisoning in metal-based catalysts, leading to their deactivation by strongly adsorbing onto the active sites, thereby preventing the adsorption of reactants. Moreover, poisoning of the catalyst support, such as $Al_2O_3$, may also occur, resulting in alterations of its crystalline structure [36,53,54]. Catalyst deactivation associated with the presence of phosphate species has been investigated predominantly in the field of electrocatalysis. Extensive studies on high temperature proton exchange membrane fuel cells have demonstrated that phosphoric acid and phosphate species can strongly interact with catalytic surface, acting as a catalyst poison through strong adsorption on active sites, as evidenced by in-operando spectroscopic analyses [55,56]. The influence of such anions was also investigated herein to elucidate their potential role in APR catalyst deactivation and decouple fouling-driven mechanisms from additional contributions.

To this end, an ion-exchange pretreatment was carried out using a resin on the 1:18 diluted feed. Under these conditions, sulfate and phosphate concentrations were 15 and 132 mg/L, respectively. The amount of resin was optimized to selectively remove the desired anion. Using 0.4 mg/mL of resin, complete sulfate removal was reached after 150 min. Following adsorption, the aqueous phase was subjected to the APR test, and no substantial difference was observed compared to the untreated test in terms of hydrogen productivity and CtoG conversion (Fig. 6-A). Also, the composition of the gas phase remained essentially unchanged (Fig. 6-B), the TOC removal amounted to 35% and 37% for the tests without and with sulfate adsorption, respectively, and HPLC/GC-MS analyses did not reveal any substantial differences. Based on these results, it was evident that the sulfate ion did not induce catalyst deactivation under these specific operating conditions.

As observed in previous tests performed without any pretreatment, phosphate was not detected in the liquid phase after APR reaction. This was consistent with FE-SEM and XPS characterization of the spent catalyst (Section 3.4), which revealed the presence of phosphate ions deposited on the catalyst surface. Based on these results, 1 g of resin was employed to reach the complete adsorption of sulfate and phosphate after 90 min. This pretreatment led to a marked enhancement in APR performance, with $H_2$ productivity reaching 30 mmol $H_2/g_C$, and carbon to gas conversion increasing to 40% (Fig. 6-A). The gas phase composition showed an increase in hydrogen content, coupled to a decrease in $CO_2$ production, which reached 35% (Fig. 6-B). An increase in TOC removal was observed, reaching 62%. Complete conversion was achieved for glycerol, as well as for cyclic ketones, 2-pyrrolidinone and 6-methyl-3-pyridinol, whereas acetic and propionic acid showed no significant conversion. Overall, the strong performance improvement achieved after phosphate adsorption indicates its major role in catalyst deactivation. Future work should systematically address adsorption isotherms, kinetics, and resin recyclability, as these aspects are essential to clarify the adsorption mechanism and evaluate process feasibility under realistic operating conditions.

### 3.3.3. *Catalyst deactivation*

Spent catalysts employed in the reaction preceded by pretreatments

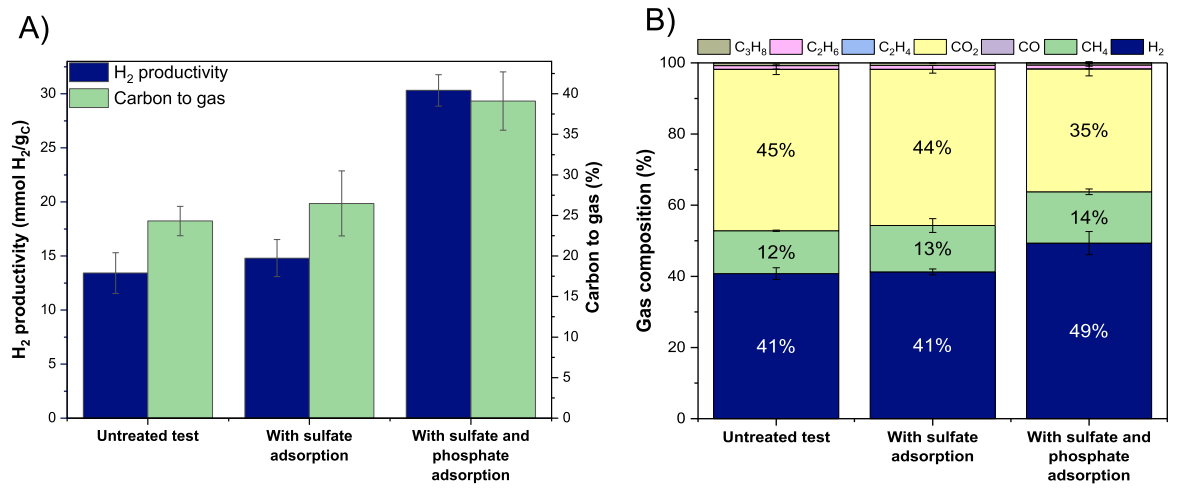


**Fig. 6.** Influence of adsorption pretreatment on $H_2$ productivity, carbon to gas (A) and gas composition (B), obtained from the APR of HTC-AP. Reaction conditions: 400 mg $Ru/Al_2O_3$, 270 °C, 1 h, 1:18 dilution rate.

were also tested in the APR of glycolic acid to assess the deactivation process in detail. Fig. 7 shows the results for those spent catalysts and compares their behavior with that of fresh $Ru/Al_2O_3$ under the same APR conditions. For the sake of comparison, the results obtained for the untreated tests are also reported.

Thermal pretreatment resulted in an overall improvement in catalyst stability. Although the catalyst recovered from the 1:3 test exhibited the lowest performance among the pretreated samples, it still represented a clear improvement with respect to the spent catalyst obtained from the test without preheating: hydrogen productivity increased to 16 mmol $H_2/g_C$ from 3 mmol $H_2/g_C$ previously obtained, and with a simultaneous glycolic acid conversion increased from 3% to 11%.

In the 1:18 dilution ratio, even though the thermal pretreatment did not result in significant solid formation, the spent catalyst slightly improved the reaction performance. However, it is worth noting that glycolic acid conversion was approximately half of that achieved with the fresh catalyst. These observations suggested that catalyst deactivation could not be exclusively attributed to solid formation, and additional factors, such as dissolved inorganics species in the reaction medium, cannot be excluded. As a matter of fact, increased dilution would result also in a lower concentration of sulfur- and phosphorus-containing compounds, which would have interacted to a lower extent with the catalyst surface.

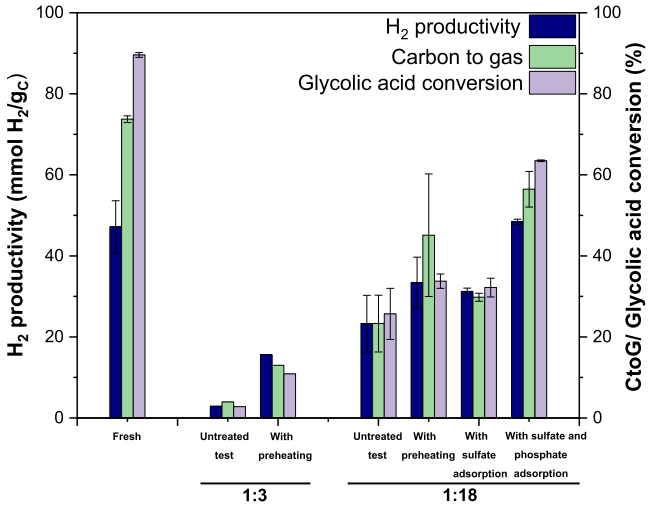


**Fig. 7.** $H_2$ productivity, carbon to gas and glycolic acid conversion, obtained from APR reactions of glycolic acid performed with different spent catalysts. Reaction conditions: 100 mg $Ru/Al_2O_3$, 270 °C, 1 h, 1 wt% glycolic acid.

Consistent with the unchanged APR performance observed after sulfate adsorption (Fig. 6), the corresponding spent catalyst also showed no significant improvement during glycolic APR. On the other hand, the spent catalyst from the reaction preceded by sulfate and phosphate adsorption demonstrated a reduced deactivation. Hydrogen productivity reached the same level as that obtained with the fresh catalyst, while CtoG and glycolic acid conversion were equal to 56% and 65% respectively, showing less pronounced differences from the values measured with fresh $Ru/Al_2O_3$.

As described in Section 3.2.3, a deviation between hydrogen productivity and glycolic acid conversion was also observed in these tests. In the test preceded by sulfate and phosphate adsorption, even though the absolute amount of hydrogen produced was comparable to that obtained with the fresh catalyst, glycolic acid did not achieve the same level of conversion. A similar trend was observed in the pretreated tests: in the 1:18 experiment, $H_2$ productivity decreased by only 12%, whereas glycolic acid conversion dropped by 50%. These findings suggested that, despite the pretreatments, certain species may have remained adsorbed on the catalyst surface, contributing to hydrogen formation and not being removed through thermal pretreatment. Further investigation will be performed to investigate this hypothesis, but preliminary results were reported in Section 3.4.

### 3.4. Catalyst characterization

To achieve a better understanding of the phenomena responsible for catalyst deactivation, characterization analyses were performed on both fresh and spent catalysts.

The surface area of the fresh $Ru/Al_2O_3$ catalyst was 110.7 $m^2/g$, with a pore volume of 0.232 $cm^3/g$. Following the APR test carried out at 270 °C, with a carbon concentration of 1.7 g/L and without any pretreatment, the spent catalyst exhibited a 13% decrease in surface area and a 17% reduction in pore volume. These decreases could be attributed to the deposition of organic and inorganic species on the catalyst surface, leading to a partial occlusion of the pore structure. Literature sometimes reports more pronounced loss of surface area under APR conditions. In particular, studies on the APR of sugar-derived compounds have shown reductions in catalyst surface area of up to 90%, mainly attributed to the formation of solid carbonaceous deposits on the catalyst surface, leading to its deactivation [39,57]. The APR of 1% alginate solution led to a 30% decrease in the surface area of the used catalyst [58]. Despite not severe herein, such worsening of textural

properties can be meaningful, in particular if compared with the spent catalyst from APR of glycolic acid, where no change in surface area was observed (114.3 $m^2/g$). The spent catalyst of the untreated test was subsequently subjected to a washing treatment in distilled water at 270 °C for 1 h, to evaluate the potential removal of deposited species through solubilization into aqueous phase. During this APR-like washing step, a gaseous phase was produced, consisting of 61% $H_2$, 24% $CO_2$, and 14% $CH_4$. In absolute terms, hydrogen production amounted to about 85% of the one generated during the previous untreated test itself. These results were in agreement with the interpretation reported in Section 3.3.3, indicating that the reduction in surface area and pore volume may be associated with the presence of adsorbed species that could still undergo conversion under APR conditions. After this washing step, the catalyst still showed a slightly lower surface area reduction of 10% and pore volume decrease of 15% with respect to the fresh sample, indicating only a partial removal of the deposited species. Although no systematic regeneration study was performed in the present work, preliminary reuse tests after an intermediate APR-like treatment with glycolic acid suggested a slight recovery of catalytic performance, which may be consistent with the partial removal of deposited phosphate species under hydrothermal conditions and further supports the need for dedicated regeneration studies.

Thermogravimetric analysis of the fresh $Ru/Al_2O_3$ catalyst, shown in Fig. 8-A and B, revealed a total weight loss of 6.5%. The first weight loss, observed below 150 °C, was attributed to the removal of adsorbed water from the catalyst surface and pores. A further gradual weight reduction was ascribed to the dehydroxylation of the $\gamma$-$Al_2O_3$ support, involving condensation of surface hydroxyl groups and release of water [59]. TGA of the spent catalysts from the untreated test and from the test preceded by thermal treatment, performed with a dilution ratio of 1:18 and at 270 °C, was also performed. In both cases, an initial weight loss (25-150 °C) was observed and was attributed to the absorbed water. A

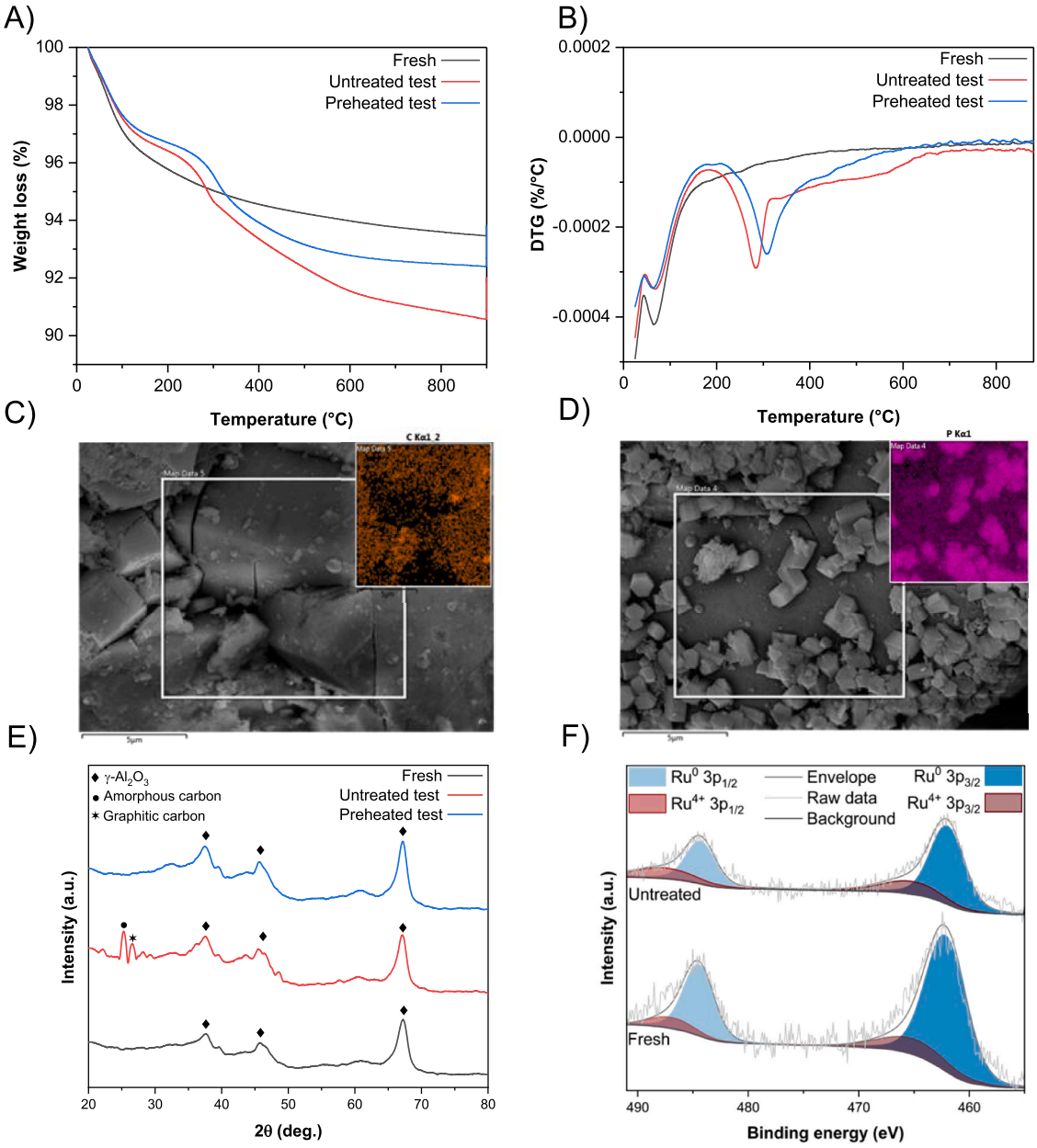


**Fig. 8.** Thermogravimetric (A) and differential thermogravimetric (B) analysis of fresh catalyst and spent catalyst after APR; FE-SEM images of the spent catalysts after APR performed without pretreatment (C) and after APR performed with sulfate adsorption (D); XRD analysis of fresh and spent catalysts (E); XPS spectra of Ru 3p of fresh and spent catalyst (F).

second weight loss occurred between approximately 250 °C and 600 °C, and two main hypotheses can explain its presence. It could be associated with the transformation of boehmite into alumina, a process involving dehydroxylation and water release. In fact, transition alumina-boehmite is a phenomenon commonly reported for alumina-based materials exposed to hydrothermal environments [40,60]. However, it has been demonstrated that the presence of organic molecules may affect the transformation pathways, preventing hydrolysis and formation of boehmite [60,61]. Furthermore, XRD analyses (Fig. 8-E) of the same spent catalyst did not reveal diffraction peaks attributable to crystalline boehmite, with characteristic peaks at 28°, 38.2° and 49° [62]. In light of these observations, the weight loss may be mostly associated with the thermal decomposition and desorption of adsorbed species and carbonaceous deposits formed during APR. The spent catalyst obtained from the untreated reaction exhibited a higher overall weight loss (10%) compared to the one obtained from the pretreated sample. This trend was consistent with the deactivation phenomenon and slight improvement discussed in Section 3.3.3 and suggested a higher accumulation of carbonaceous species on the catalyst surface in the absence of pretreatment.

The XRD of fresh and spent catalysts exhibited diffraction peaks at $2\theta = 37.7°$, 45.8°, and 66.8°, which can be attributed to the (311), (400), and (440) diffraction planes of $\gamma$-$Al_2O_3$ [63–65]. No distinct diffraction peaks attributable to crystalline Ru were observed in the XRD patterns. This suggested a high dispersion of Ru species on the support. The analyses of the spent catalyst used in the untreated reaction revealed diffraction peaks at 25.3° and 26.7° (Fig. 8-E). The first one was consistent with the angular range commonly reported for turbostratic or amorphous carbon [66,67], while the second could be assigned to the (002) plane of crystalline graphitic carbon [68].

The surface morphology of the spent catalysts was analyzed by FE-SEM coupled with EDX mapping. The surface of the spent catalyst obtained from the APR reaction preceded by sulfate adsorption was characterized by the presence of C-rich microspheres (Fig. 8-C). Elemental analysis confirmed a carbon concentration in the spent catalyst of 9 wt %, and the shape of these structures appeared to be consistent with secondary char, corelated with an aqueous phase degradation of biomass followed by the polymerization of organic molecules into a solid phase [69–71]. It was observed to manifest characteristically as microspherical particles, adhering to the surface of the primary char [72]. A markedly more pronounced formation of carbon-rich microspheres was observed on the spent catalyst recovered after APR performed with the untreated feed under the most concentrated condition, where extensive carbon deposition covered large portions of the catalyst surface (Fig. S7–A). Elemental analysis of this sample indicated a carbon content of 17 wt%, providing quantitative evidence of the significant carbon accumulation observed on the catalyst surface, as well as nitrogen presence (approximately 1 wt%), suggesting the incorporation of nitrogen-containing Maillard-derived organic species within the carbonaceous deposits. These observations further support that high organic load promotes polymerization and carbon deposition during APR, contributing to catalyst deactivation under concentrated conditions. Elemental analysis also revealed contents below 1 wt% for magnesium, silicon and calcium. The presence of phosphorus on the catalyst surface, accounting for 4%, is clearly shown in Fig. 8-D, which reports Ru/$Al_2O_3$ recovered after reaction performed without any pretreatment at 270 °C using the 1:18 dilution. The nature of the phosphorus species was further investigated in order to clarify their possible role in catalyst deactivation. Hydrothermal conditions such as those encountered during APR may promote the formation of aluminum phosphate phases; however, their development is generally associated with well-defined synthesis conditions that differ from those applied in the present system [73,74]. In the present case, XRD analysis did not reveal any diffraction features attributable to aluminophosphate phases. Consistently, XPS results showed Al 2p and O 1s binding energies (74.3 eV and 531 eV, respectively) characteristic of $\gamma$- $Al_2O_3$, with no evidence of the shifts typically reported for $AlPO_4$-related species [75]. These results indicated that phosphorus was not incorporated into a distinct crystalline phase. Instead, phosphorus was more likely present as highly dispersed surface species. In this regard, phosphate groups are known to interact with $\gamma$-$Al_2O_3$ via surface hydroxyl functionalities, leading to the formation of Al–O–P linkages without the development of bulk aluminophosphate phases [76]. Further insight was provided by FESEM-EDX analysis of a catalyst recovered after APR performed under more concentrated conditions and following thermal pretreatment. In this case, the phosphorus-containing phase exhibited a more defined morphology, with polyhedral structures enriched in phosphorus and associated lamellar regions containing minor amounts of magnesium (Fig. S7–B). The spatial distribution of these elements, together with the observed morphologies, is consistent with the formation of Mg–P deposits typically associated with precipitation processes in aqueous systems. Although their precise structural nature could not be conclusively determined, these observations suggest that, under more severe conditions, phosphorus deposition may also proceed via precipitation pathways involving Mg–P species. Based on these observations, phosphorus deposition can be ascribed to both surface interactions with the support and, under more severe conditions, the formation of secondary inorganic deposits, thereby indicating the coexistence of multiple deposition pathways. Finally, in order to get insights on the superficial state of the active metal, XPS analysis confirmed the presence of phosphorus and magnesium species on the catalyst surface (Fig. S8). The high resolution XPS spectra of Ru 3p, reported in Fig. 8-F, showed no significant binding energy shifts between the fresh and spent catalysts, indicating that the superficial oxidation state of the active Ru species remained largely unchanged during APR. Overall, the combined catalytic results and post-reaction characterization allow a first semi-quantitative assessment of the deactivation routes. Under the diluted condition (1:18), the loss in glycolic acid conversion from ca. 90% for the fresh catalyst to ca. 25% for the spent one cannot be explained by pore blockage alone, since the corresponding decreases in surface area and pore volume were limited to 13% and 17%, respectively. Thermal pretreatment, which did not modify the inorganic composition of the feed, restored only about 10 absolute percentage points of glycolic acid conversion (i.e., approximately 15% of the total activity loss), indicating a secondary but non-negligible contribution of carbonaceous deposition and/or adsorbed organics. By contrast, sulfate adsorption alone produced no appreciable effect, whereas combined sulfate and phosphate removal restored about 40 absolute percentage points of glycolic acid conversion (i.e., approximately 60% of the total loss), indicating that phosphorus-related surface deactivation is the dominant mechanism at low carbon loading. Under concentrated-feed conditions (1:3), the persistence of substantial solid formation even after preheating indicates that carbonaceous deposition, physical coverage, and phosphorus-related effects coexisted, so that their individual contributions cannot be reliably disentangled from the present dataset.

## 4. Conclusion

In this study, aqueous-phase reforming of the wastewater produced by hydrothermal carbonization of *Chlorella sorokiniana* was investigated. Process-water characterization identified the dominant organic constituents (glycerol, acetic acid, and propionic acid) together with relevant inorganic species, including Na-, S-, and P-containing compounds. The effects of initial carbon concentration and reaction temperature were systematically assessed in terms of $H_2$ productivity and carbon conversion to gas. At high initial TOC, approximately 25% of the initial TOC was converted into a solid fraction during APR, which correlated with a marked deterioration in $H_2$ production. Conversely, increasing reaction temperature consistently improved reforming outcomes, with $H_2$ productivity rising from 6 to 13 mmol $H_2/g_C$ and carbon conversion to gas increasing from ca. 3% to 25% across the investigated temperature window. Catalyst deactivation was elucidated through a wide

characterization, which indicated concurrent carbon deposition and accumulation of phosphorus-containing species on the catalyst surface. The impact of deactivation was further isolated using glycolic acid as a probe molecule: glycolic acid conversion decreased from about 90% for the fresh catalyst to 3% after exposure to high-TOC wastewater, and to 25% after low-TOC operation, confirming the strong dependence of deactivation severity on feed composition. Guided by these mechanistic insights, two mitigation strategies were explored: (i) thermal pretreatment to partially remove carbonaceous deposits, and (ii) upstream selective adsorption of inorganic species to limit inorganic-driven deactivation. These approaches substantially improved the hydrogen productivity (+130%) and catalyst reusability, increasing glycolic acid conversion to about 45% after thermal pretreatment and to 60% after phosphate adsorption. Overall, this work demonstrates that the aqueous-phase composition governs APR performance not only through its organic fraction but also, and critically, through inorganic presence, with phosphates emerging as a key deactivation driver. Further tests at longer reaction times are needed to assess how pretreatments influence the kinetic evolution of APR and to clarify whether the limited conversion of residual compounds is related to their recalcitrant nature, which may require more severe operating conditions for effective removal. Future work will extend these findings to continuous APR operation to evaluate long-term stability, regeneration requirements, and process robustness under undiluted realistic conditions.

## CRediT authorship contribution statement

**Marina Andriolo:** Conceptualization, Data curation, Formal analysis, Investigation, Methodology, Writing – original draft, Writing – review & editing. **Edoardo Tito:** Conceptualization, Formal analysis, Methodology, Validation, Writing – original draft, Writing – review & editing. **Giuseppe Pipitone:** Conceptualization, Data curation, Formal analysis, Methodology, Project administration, Supervision, Validation, Writing – original draft, Writing – review & editing. **Raffaele Pirone:** Conceptualization, Funding acquisition, Project administration, Supervision. **Samir Bensaid:** Conceptualization, Formal analysis, Funding acquisition, Methodology, Project administration, Supervision, Validation, Writing – review & editing.

## Declaration of competing interest

The authors declare the following financial interests/personal relationships which may be considered as potential competing interests: Samir Bensaid reports financial support was provided by European Union. If there are other authors, they declare that they have no known competing financial interests or personal relationships that could have appeared to influence the work reported in this paper.

## Acknowledgements

The project leading to this research has received funding from the European Union under grant agreement N° 101146861. The authors acknowledge Enrico Sartoretti for FE-SEM and XPS measurements, and Camilla Galletti for ICP and XRD characterization.

## Appendix A. Supplementary data

Supplementary data to this article can be found online at https://doi.org/10.1016/j.ijhydene.2026.155972.

## References

[1] Funke A, Ziegler F. Hydrothermal carbonization of biomass: a summary and discussion of chemical mechanisms for process engineering. Biofuel Bioprod Biorefining 2010;4. https://doi.org/10.1002/bbb.198.

[2] Heilmann SM, Davis HT, Jader LR, Lefebvre PA, Sadowsky MJ, Schendel FJ, von Keitz MG, Valentas KJ. Hydrothermal carbonization of microalgae. Biomass Bioenergy 2010;34:875–82. https://doi.org/10.1016/j.biombioe.2010.01.032.

[3] Wang T, Zhai Y, Zhu Y, Li C, Zeng G. A review of the hydrothermal carbonization of biomass waste for hydrochar formation: process conditions, fundamentals, and physicochemical properties. Renew Sustain Energy Rev 2018;90:223–47. https://doi.org/10.1016/j.rser.2018.03.071.

[4] Kozyatnyk I, Benavente V, Weidemann E, Gentili FG, Jansson S. Influence of hydrothermal carbonization conditions on the porosity, functionality, and sorption properties of microalgae hydrochars. Sci Rep 2023;13:1–10. https://doi.org/10.1038/s41598-023-35331-0.

[5] Miyata Y, Fukushima T, Kihira M, Takisawa K. Effect of hydrothermal reaction conditions on hydrochar from microalgae. Biomass Convers Biorefinery 2024;14:349–57. https://doi.org/10.1007/s13399-021-02275-2.

[6] Khoo CG, Lam MK, Mohamed AR, Lee KT. Hydrochar production from high-ash low-lipid microalgal biomass via hydrothermal carbonization: effects of operational parameters and products characterization. Environ Res 2020;188:109828. https://doi.org/10.1016/j.envres.2020.109828.

[7] Belete YZ, Leu S, Boussiba S, Zorin B, Posten C, Thomsen L, Wang S, Gross A, Bernstein R. Characterization and utilization of hydrothermal carbonization aqueous phase as nutrient source for microalgal growth. Bioresour Technol 2019;290:121758. https://doi.org/10.1016/j.biortech.2019.121758.

[8] Marin-Batista JD, Villamil JA, Rodriguez JJ, Mohedano AF, de la Rubia MA. Valorization of microalgal biomass by hydrothermal carbonization and anaerobic digestion. Bioresour Technol 2019;274:395–402. https://doi.org/10.1016/j.biortech.2018.11.103.

[9] Heidari M, Dutta A, Acharya B, Mahmud S. A review of the current knowledge and challenges of hydrothermal carbonization for biomass conversion. J Energy Inst 2019;92:1779–99. https://doi.org/10.1016/j.joei.2018.12.003.

[10] Gou L, Dai L, Wang Y. Coupling of struvite crystallization and aqueous phase recirculation for hydrochar upgrading and nitrogen recovery during hydrothermal carbonization of sewage sludge. Sci Total Environ 2024;929:172682. https://doi.org/10.1016/j.scitotenv.2024.172682.

[11] Nguyen TAH, Bui TH, Guo WS, Ngo HH. Valorization of the aqueous phase from hydrothermal carbonization of different feedstocks: challenges and perspectives. Chem Eng J 2023;472:144802. https://doi.org/10.1016/j.cej.2023.144802.

[12] Broch A, Jena U, Hoekman SK, Langford J. Analysis of solid and aqueous phase products from hydrothermal carbonization of whole and lipid-extracted algae. Energies 2014;7:62–79. https://doi.org/10.3390/en7010062.

[13] Zoppi G, Pipitone G, Pirone R, Bensaid S. Aqueous phase reforming process for the valorization of wastewater streams: application to different industrial scenarios. Catal Today 2022;387:224–36. https://doi.org/10.1016/j.cattod.2021.06.002.

[14] Cortright RD, Davda RR, Dumesic JA. Hydrogen from catalytic reforming of biomass-derived hydrocarbons in liquid water. Nature 2002;418:964–7. https://doi.org/10.1038/nature01009.

[15] Davda RR, Shabaker JW, Huber GW, Cortright RD, Dumesic JA. A review of catalytic issues and process conditions for renewable hydrogen and alkanes by aqueous-phase reforming of oxygenated hydrocarbons over supported metal catalysts. Appl Catal B Environ 2005;56:171–86. https://doi.org/10.1016/j.apcatb.2004.04.027.

[16] Pipitone G, Zoppi G, Pirone R, Bensaid S. A critical review on catalyst design for aqueous phase reforming. Int J Hydrogen Energy 2022;47:151–80. https://doi.org/10.1016/j.ijhydene.2021.09.206.

[17] Justicia J, Heras F, Moreno I, Baeza JA, Calvo L, Fermoso J, Gilarranz MA. Understanding the relationship between catalytic pyrolysis conditions and hydrogen production by aqueous phase reforming of the water-soluble fractions of bio-oils. Energy Convers Manag 2024;320. https://doi.org/10.1016/j.enconman.2024.118999.

[18] Yu Y, Wang Y, Chen C, Bu Q, Tao J, Jia X, Sun J, Yan B, Chen G. Pollutant degradation and hydrogen production of landfill leachate membrane concentrates via aqueous phase reforming. Chemosphere 2024;364. https://doi.org/10.1016/j.chemosphere.2024.143027.

[19] Torres M, Justicia J, Baeza JA, Calvo L, Heras F, Gilarranz MA. Hydrogen production from pruning waste biomass by integration of hydrothermal treatment and aqueous phase reforming. Int J Hydrogen Energy 2024;63:142–50. https://doi.org/10.1016/j.ijhydene.2024.03.182.

[20] Justicia J, Baeza JA, Calvo L, Heras F, Gilarranz MA. Valorization to hydrogen of bio-oil aqueous fractions from lignocellulosic biomass pyrolysis by aqueous phase reforming over Pt/C catalyst. Chem Eng J 2023;477. https://doi.org/10.1016/j.cej.2023.146860.

[21] Wang J, Chen Y, Zhao W, Liang R, Yan B, Tao J, Su H, Chen G. Influence of calcination temperature on the evolution of α-MoO3 nanosheets catalyst for aqueous phase reforming of biogas slurry. Fuel 2023;345:128074. https://doi.org/10.1016/j.fuel.2023.128074.

[22] Tito E, Zoppi G, Pipitone G, Miliotti E, Di Fraia A, Rizzo AM, Pirone R, Chiaramonti D, Bensaid S. Conceptual design and techno-economic assessment of coupled hydrothermal liquefaction and aqueous phase reforming of lignocellulosic residues. J Environ Chem Eng 2023;11:109076. https://doi.org/10.1016/j.jece.2022.109076.

[23] Zoppi G, Tito E, Bianco I, Pipitone G, Pirone R, Bensaid S. Life cycle assessment of the biofuel production from lignocellulosic biomass in a hydrothermal liquefaction – aqueous phase reforming integrated biorefinery. Renew Energy 2023;206:375–85. https://doi.org/10.1016/j.renene.2023.02.011.

[24] Öztürk Y, Ekmekçi Z. Removal of sulfate ions from process water by ion exchange resins. Miner Eng 2020;159:106613. https://doi.org/10.1016/j.mineng.2020.106613.

[25] Feng D, Aldrich C, Tan H. Treatment of acid mine water by use of heavy metal precipitation and ion exchange. Miner Eng 2000;13:623–42. https://doi.org/10.1016/S0892-6875(00)00045-5.
[26] Tsarpali M, Arora N, Kuhn JN, Philippidis GP. Beneficial use of the aqueous phase generated during hydrothermal carbonization of algae as nutrient source for algae cultivation. Algal Res 2021;60:102485. https://doi.org/10.1016/j.algal.2021.102485.
[27] Celletti S, Lanz M, Bergamo A, Benedetti V, Basso D, Baratieri M, Cesco S, Mimmo T. Evaluating the aqueous phase from hydrothermal carbonization of cow manure digestate as possible fertilizer solution for plant growth. Front Plant Sci 2021;12. https://doi.org/10.3389/fpls.2021.687434.
[28] Liu X, Ai N, Zhang H, Lu M, Ji D, Yu F, Ji J. Quantification of glucose, xylose, arabinose, furfural, and HMF in corncob hydrolysate by HPLC-PDA-ELSD. Carbohydr Res 2012;353:111–4. https://doi.org/10.1016/j.carres.2012.03.029.
[29] Givry S, Bliard C, Duchiron F. Selective ketopentose analysis in concentrate carbohydrate syrups by HPLC. Carbohydr Res 2007;342:859–64. https://doi.org/10.1016/j.carres.2006.12.013.
[30] Scarlata CJ, Hyman DA. Development and validation of a fast high pressure liquid chromatography method for the analysis of lignocellulosic biomass hydrolysis and fermentation products. J Chromatogr A 2010;1217:2082–7. https://doi.org/10.1016/j.chroma.2010.01.061.
[31] Levine RB, Sierra COS, Hockstad R, Obeid W, Hatcher PG, Savage PE. The use of hydrothermal carbonization to recycle nutrients in algal biofuel production. Environ Prog Sustain Energy 2013;32. https://doi.org/10.1002/ep.11812.
[32] Borrero-López AM, Masson E, Celzard A, Fierro V. Modelling the reactions of cellulose, hemicellulose and lignin submitted to hydrothermal treatment. Ind Crops Prod 2018;124:919–30. https://doi.org/10.1016/j.indcrop.2018.08.045.
[33] Wang R, Lin Z, Peng P, Tan S, Zhao Z, Yin Q, Wang C. Influence mechanism of aqueous organic components on the hydrochar formation reaction during the biomass hydrothermal carbonization wastewater recycling. Fuel 2022;326:125033. https://doi.org/10.1016/j.fuel.2022.125033.
[34] Maddi B, Panisko E, Wietsma T, Lemmon T, Swita M, Albrecht K, Howe D. Quantitative characterization of the aqueous fraction from hydrothermal liquefaction of algae. Biomass Bioenergy 2016;93:122–30. https://doi.org/10.1016/j.biombioe.2016.07.010.
[35] Gai C, Zhang Y, Chen WT, Zhou Y, Schideman L, Zhang P, Tommaso G, Kuo CT, Dong Y. Characterization of aqueous phase from the hydrothermal liquefaction of Chlorella pyrenoidosa. Bioresour Technol 2015;184:328–35. https://doi.org/10.1016/j.biortech.2014.10.118.
[36] Zhang X, Zhou Y, Li G, Zhang L, Yin C, Yang Y, Wang H, Feng F, Wei L, Zhang Q, Yang F, Lin L, Lu C, Li X. A highly sulfur resistant and stable heterogeneous catalyst for liquid-phase hydrogenation. Appl Catal B Environ 2022;315:121566. https://doi.org/10.1016/j.apcatb.2022.121566.
[37] López Barreiro D, Riede S, Hornung U, Kruse A, Prins W. Hydrothermal liquefaction of microalgae: effect on the product yields of the addition of an organic solvent to separate the aqueous phase and the biocrude oil. Algal Res 2015;12:206–12. https://doi.org/10.1016/j.algal.2015.08.025.
[38] Oliveira AS, Sarrión A, Baeza JA, Diaz E, Calvo L, Mohedano AF, Gilarranz MA. Integration of hydrothermal carbonization and aqueous phase reforming for energy recovery from sewage sludge. Chem Eng J 2022;442. https://doi.org/10.1016/j.cej.2022.136301.
[39] Pipitone G, Zoppi G, Frattini A, Bocchini S, Pirone R, Bensaid S. Aqueous phase reforming of sugar-based biorefinery streams: from the simplicity of model compounds to the complexity of real feeds. Catal Today 2020;345:267–79. https://doi.org/10.1016/j.cattod.2019.09.031.
[40] Pipitone G, Zoppi G, Ansaloni S, Bocchini S, Deorsola FA, Pirone R, Bensaid S. Towards the sustainable hydrogen production by catalytic conversion of C-laden biorefinery aqueous streams. Chem Eng J 2019;377:120677. https://doi.org/10.1016/j.cej.2018.12.137.
[41] Pipitone G, Hensley AJR, Omoniyi A, Zoppi G, Pirone R, Bensaid S. Unravelling competitive adsorption phenomena in the aqueous phase reforming of carboxylic acids on Pt catalysts: an experimental and theoretical study. Chem Eng J 2024;482:148902. https://doi.org/10.1016/j.cej.2024.148902.
[42] Justicia J, Alberto Baeza J, de Oliveira AS, Calvo L, Heras F, Gilarranz MA. Aqueous-phase reforming of water-soluble compounds from pyrolysis bio-oils. Renew Energy 2022;199:895–907. https://doi.org/10.1016/j.renene.2022.09.021.
[43] Oliveira AS, Baeza JA, Calvo L, Gilarranz MA. Aqueous phase reforming of starch wastewater over Pt and Pt-based bimetallic catalysts for green hydrogen production. Chem Eng J 2023;460. https://doi.org/10.1016/j.cej.2023.141770.0–11.
[44] Oliveira AS, Cordero-Lanzac T, Baeza JA, Calvo L, Rodriguez JJ, Gilarranz MA. Continuous aqueous phase reforming of wastewater streams: a catalyst deactivation study. Fuel 2021;305:121506. https://doi.org/10.1016/j.fuel.2021.121506.
[45] Joshi AN, Vaidya PD. Hydrogen production by aqueous phase reforming of synthetic sewage using Pt/C catalyst: effect of reaction parameters and pre-treatment strategies. Waste Biomass Valoriz 2024;15:805–19. https://doi.org/10.1007/s12649-023-02187-4.
[46] Pipitone G, Zoppi G, Bocchini S, Maria A, Chiaramonti D. Aqueous phase reforming of the residual waters derived from lignin-rich hydrothermal liquefaction : investigation of representative organic compounds and actual biore fi nery streams. 345237–250, https://doi.org/10.1016/j.cattod.2019.09.040; 2020.
[47] Park C, Jung E. Comparison of microalgal hydrochar and pyrochar : production , physicochemical properties , and environmental application. Environ Sci Pollut Res 2024;31:2521–32. https://doi.org/10.1007/s11356-023-31317-7.
[48] Shi N, Liu Q, He X, Wang G, Chen N, Peng J, Ma L. Molecular structure and formation mechanism of hydrochar from hydrothermal carbonization of carbohydrates. https://doi.org/10.1021/acs.energyfuels.9b02174; 2019.
[49] Liu T, Jiao HT, Yang L, Zhang W, Hu Y, Guo Y, Yang L, Leng S, Chen J, Chen J, Peng H, Leng L, Zhou W. Co-hydrothermal carbonization of cellulose, hemicellulose, and protein with aqueous phase recirculation: insight into the reaction mechanisms on hydrochar formation. Energy 2022;251:123965. https://doi.org/10.1016/j.energy.2022.123965.
[50] Maruani V, Narayanin-richenapin S, Framery E, Andrioletti B, De Lyon U, Claude U, Lyon B, Umr I, Novembre B, Villeurbanne F-. Acidic hydrothermal dehydration of. 2–8, https://doi.org/10.1021/acssuschemeng.8b03479; 2018.
[51] Sevilla M, Fuertes AB. The production of carbon materials by hydrothermal carbonization of cellulose. Carbon N Y 2009;47:2281–9. https://doi.org/10.1016/j.carbon.2009.04.026.
[52] Rasmussen H, Sørensen HR, Meyer AS. Formation of degradation compounds from lignocellulosic biomass in the biorefinery: sugar reaction mechanisms. Carbohydr Res 2014;385:45–57. https://doi.org/10.1016/j.carres.2013.08.029.
[53] Nasri NS, Jones JM, Dupont VA, Williams A. A comparative study of sulfur poisoning and regeneration of precious-meted catalysts. Energy Fuels 1998;12:1130–4. https://doi.org/10.1021/ef980104j.
[54] Argyle MD, Bartholomew CH. Heterogeneous catalyst deactivation and regeneration: a review. Catalysts 2015;5:145–269. https://doi.org/10.3390/catal5010145.
[55] Xue D, Zhang J-N. Recent progress of antipoisoning catalytic materials for high temperature proton exchange membrane fuel cells doped with phosphoric acid. Ind Chem Mater 2024;2:173–90. https://doi.org/10.1039/d3im00101f.
[56] Kaserer S, Caldwell KM, Ramaker DE, Roth C. Analyzing the influence of H3PO4 as catalyst poison in high temperature PEM fuel cells using in-operando X-ray absorption spectroscopy. J Phys Chem C 2013;117:6210–7. https://doi.org/10.1021/jp311924q.
[57] Pipitone G, Pirone R, Bensaid S. Aqueous phase reforming of dairy wastewater for hydrogen production : an experimental and energetic assessment. 2024.
[58] Pipitone G, Tosches D, Bensaid S, Galia A. Valorization of alginate for the production of hydrogen via catalytic aqueous phase reforming. 304153–164, https://doi.org/10.1016/j.cattod.2017.09.047; 2018.
[59] Lashdaf M, Hatanpää T, Krause AOI, Lahtinen J, Lindblad M, Tiitta M. Deposition of palladium and ruthenium β-diketonates on alumina and silica supports in gas and liquid phase. Appl Catal A Gen 2003;241:51–63. https://doi.org/10.1016/S0926-860X(02)00424-6.
[60] Jongerius AL, Copeland JR, Foo GS, Hofmann JP, Bruijnincx PCA, Sievers C, Weckhuysen BM. Stability of Pt/γ-Al2O3 catalysts in lignin and lignin model compound solutions under liquid phase reforming reaction conditions. ACS Catal 2013;3:464–73. https://doi.org/10.1021/cs300684y.
[61] Ravenelle RM, Copeland JR, Van Pelt AH, Crittenden JC, Sievers C. Stability of Pt/γ-Al 2O 3 catalysts in model biomass solutions. Top Catal 2012;55:162–74. https://doi.org/10.1007/s11244-012-9785-3.
[62] Lin JY, Lee JY, Wang CY. Alkaline-enhanced boehmite catalysts for catalytic hydrolysis of carbonyl sulfide at low temperature. Sustain Environ Res 2025;35. https://doi.org/10.1186/s42834-025-00242-4.
[63] Quindimil A, De-la-torre U, Pereda-ayo B, Davó-quiñonero A. Effect of metal loading on the CO 2 methanation : a comparison between alumina supported Ni and Ru catalysts. 356419–432, https://doi.org/10.1016/j.cattod.2019.06.027; 2020.
[64] Kim YH, Park ED. Applied catalysis B : environmental the effect of the crystalline phase of alumina on the selective CO oxidation in a hydrogen-rich stream over Ru/Al 2 O 3. Appl Catal B Environ 2010;96:41–50. https://doi.org/10.1016/j.apcatb.2010.02.001.
[65] Lin B, Heng L, Fang B, Yin H, Ni J, Wang X, Lin J, Jiang L. Ammonia synthesis activity of alumina-supported ruthenium catalyst enhanced by alumina phase transformation. https://doi.org/10.1021/acscatal.8b03554; 2019.
[66] Zerin NH, Rasul MG, Jahirul MI, Sayem ASM, Quadir Z, Haque R. XRD characterization of activated carbons synthesized from tyre pyrolysis char via KOH activation. Technologies 2025;13:1–12. https://doi.org/10.3390/technologies13120565.
[67] Joshi AA, Ragupathy G. Performance and mechanisms of waste-based carbon adsorbents in heavy metal removal - an experimental and theoretical approach. RSC Adv 2025;15:34609–34. https://doi.org/10.1039/d5ra03863d.
[68] Yamagishi T, Shibutani S, Yamauchi S. Raman and XRD characterization of carbon structures in Fe-, Co-, and Ni-loaded woody charcoal: formation and growth of graphene-like layers. J Wood Sci 2025;71. https://doi.org/10.1186/s10086-025-02242-9.
[69] Pecchi M, Baratieri M, Maag AR, Goldfarb JL. Uncovering the transition between hydrothermal carbonization and liquefaction via secondary char extraction: a case study using food waste. Waste Manag 2023;168:281–9. https://doi.org/10.1016/j.wasman.2023.06.009.
[70] Lucian M, Volpe M, Gao L, Piro G, Goldfarb JL, Fiori L. Impact of hydrothermal carbonization conditions on the formation of hydrochars and secondary chars from the organic fraction of municipal solid waste. Fuel 2018;233:257–68. https://doi.org/10.1016/j.fuel.2018.06.060.
[71] Fu H, Wang F, Liu Z, Duan X, Wang L, Yi W, Zhang D. Role of secondary char on the fuel properties and pyrolysis behaviors of hydrochars: effect of temperature and liquid-solid ratio. Fuel Process Technol 2025;267. https://doi.org/10.1016/j.fuproc.2024.108167.
[72] Shen Q, Zhu X, Peng Y, Xu M, Huang Y, Xia A, Zhu X, Liao Q. Structure evolution characteristic of hydrochar and nitrogen transformation mechanism during co-

hydrothermal carbonization process of microalgae and biomass. Energy 2024;295: 131028. https://doi.org/10.1016/j.energy.2024.131028.
[73] Xia K, He Z, Zhou D, Lu X, Xia Q. Accelerated by a rotating hydrothermal synthesis route †. 24171–24174, https://doi.org/10.1039/c9ra04842a; 2019.
[74] Murayama N, Okajima N, Yamaoka S, Yamamoto H, Shibata J. Hydrothermal synthesis of AlPO 4 -5 type zeolitic materials by using aluminum dross as a raw material. 26459–462, https://doi.org/10.1016/j.jeurceramsoc.2005.06.022; 2006.
[75] Preischel F, Zanders D, Glauber J, Rönnby K, Rogalla D, Gemming T, Dement P, Nolan M, Devi A. Plasma-enhanced atomic layer deposition of AlPO4/AlPxOy: comparing dual source and supercycle approaches for composition control. 17507–17520, https://doi.org/10.1039/d5dt02282g; 2025.
[76] Roy T, Wisser D, Valero MC, Corre T, Delpoux O. Phosphate adsorption on γ - alumina: a surface complex model based on surface characterization and zeta potential measurements. https://doi.org/10.1021/acs.jpcc.0c11553; 2021.